

1

2 **Radio-magnetotelluric and controlled-source magnetotelluric surveys on a**
3 **frozen lake: opportunities for urban applications in Nordic countries**

4

5 **running title: RMT and CSAMT surveys on a frozen lake**

6 **Mehrdad Bastani^{1,2*}, Shunguo Wang³, Alireza Malehmir¹, and Suman Mehta¹⁺⁺**

7 ¹ Department of Earth Sciences, Uppsala University, SE-75236 Uppsala, Sweden

8 ² Geological Survey of Sweden, Box 670, SE-75128 Uppsala, Sweden

9 ³ Department of Electronic Systems, Norwegian University of Science and Technology, NO-
10 7491 Trondheim, Norway

11

12

13 **++ Leafymade, Stationsgatan 23, 753 40 Uppsala, Sweden**

14

15 **Acknowledgments**

16 This study was conducted within the frame of Trust 2.2 (Trust-GeoInfra; <http://www.trust->
17 geoinfra.se) sponsored by Formas (project number: 252-2012-1907), SGU (363-26512013), BeFo
18 (BeFo 340), SBUF, Skanska, FQM and NGI. We thank Torleif Dahlin and GEONOVA Consulting
19 AB along with Trafikverket for providing raw reflection seismic data (shot records) from the water
20 passages. They were processed up to stack partly along with the CSRMT survey. S. Wang thanks
21 the Norwegian Research Council and the industry partners of the GAMES consortium at NTNU
22 for financial support (grant no. 294404, 324442). We thank two anonymous reviewers along with
23 the editor for their critical reviews and suggestions that improved an earlier version of this
24 article.

25 **Abstract**

26 In a novel approach, we have carried out controlled-source and radio-magnetotelluric
27 measurements in the frequency range of 2-250 kHz on a frozen lake located over a planned major
28 multi-lane underground road tunnel near the city of Stockholm. The aim was to gain a better
29 understanding of the resistivity variations above and potentially within the crystalline bedrock.
30 Previous studies on the lake water using the boat-towed RMT technique at higher end of frequency
31 band lacked resolution at depth and could not provide conclusive information about bedrock level
32 and potential fracture systems in the bedrock. Taking advantage of Nordic winters, we measured
33 four profiles on the frozen lake complementing the previously acquired boat-towed radio-
34 magnetotelluric data utilizing a double horizontal magnetic dipole transmitter that generated
35 signals down to 1 kHz. The new resistivity models, incorporating the lower frequency data, show
36 improvements and deeper penetrations based on a combined analyses of penetration depth, data
37 misfits, and sensitivity studies. The resistivity models also show better correlation with the

38 available high-resolution shallow water reflection seismic data and the geological observations. A
39 potential fracture system within the bedrock can also better be inferred in the new models. The
40 idea of running similar surveys on frozen lakes can be further exploited in similar conditions such
41 as in Sweden where approximately seven percent of the land is covered by freshwater bodies and
42 poorly explored for infrastructure planning projects.

43

44 Keywords: frozen lake, controlled-source, electromagnetics, tunnel, radio magnetotelluric

45

46

47 Data Availability Statement: The CSRMT data collected in this study are available for further
48 research and can be collected by contacting the customer service at the Geological Survey of
49 Sweden (SGU) at: kundservice@sgu.se.

50

51

52 **Introduction**

53 It is a common practice that high resolution surface geophysical measurements are planned at areas
54 suggested by either interpretation of airborne data or other disciplines involved in a project, for
55 example geo-technicians or mine engineers. One of the challenges in planning such surveys is
56 sometimes presence of waterbodies such as lakes and rivers, which may cross or cover the target
57 structures. One such example is the 21-km-long Stockholm Bypass in Sweden where 18 km is
58 below the ground surface planned as two separate tunnels each having three lanes. The tunnels at
59 three locations pass underwater passages of the Lake Mälaren (Figure 1). Luckily, in such areas
60 the cold winters furnishes the possibility of running geophysical measurements on frozen

waterbodies. Geophysical measurements on frozen lakes and seas have been carried out over the past decades for various purposes. Gravity measurements on the surface of frozen lakes in northern parts of Europe (mainly Scandinavia) and North America is routinely conducted over the winter periods. Ugalde et al. (2006) collect gravity data at 98 stations over the frozen Wanapitei Lake in Sudbury, northern Ontario, Canada. Inclusion of the collected data into the existing database improved the Bouguer anomaly map in resolving the extent of a known meteorite crater below the central parts of the lake. Andersson and Malehmir (2018) conducted a similar survey in Sweden to find lateral extent of a carbonatite system into the Baltic Sea. Dugan et al. (2016) report the use of ground penetrating radar (GPR) to study small-scale structures within the ice covering two lakes in McMurdo Dry Valleys, Antarctica. Their findings confirmed the results from an earlier study carried out in Lake Vida where airborne transient electromagnetic (ATEM) data were also collected and modelled (Dugan et al., 2015 and reference therein). Schwamborn et al. (2002) collected high-resolution reflection seismic and GPR data over Lake Nikolay in the western Lena Delta to study the uppermost basin fill and the bordering of frozen margins. Their results showed that combination of the two profiling systems provides detailed information about stratigraphy along the profiles in both frozen and unfrozen parts of the lake.

Radio-magnetotelluric (RMT) is an established electromagnetic (EM) method for mapping near-surface resistivity variations (Tuberg et al., 1994; Tezkan et al., 2000; Bastani 2001; Persson, 2001; Bastani et al., 2012). The passive sources such as very low frequency (VLF) and LF transmitters as well as a portable data acquisition system make the RMT method efficient and practical tool for near-surface geophysical surveys. However, acquiring RMT data over shallow waterbodies pose a challenge in many conditions and in particular in the Scandinavia where a considerable portion of the land is covered by waterbodies such as rivers and lakes. To overcome some of these

84 challenges, a new acquisition technique called boat-towed RMT was introduced by Bastani et al.
85 (2015) with an example to acquire data over freshwater body of Lake Mälaren in the outskirt of
86 the city of Stockholm in Sweden over the water passages where the tunnels of Stockholm Bypass
87 cross. The EnviroMT instrument (Bastani, 2001) was modified to carry out the waterborne RMT
88 survey. The analog sensors were made to float on a wooden platform and towed by a boat at low
89 speeds (0.5-1 m/s). The boat-towed acquisition system works effectively and is highly cost-
90 effective. Mehta et al. (2017) examined and provided a detailed analysis of the resolution of boat-
91 towed RMT data. Given the frequency range of the RMT data (10-250 kHz), it was evident that
92 the RMT data acquired over Lake Mälaren provided better resolution at shallow depths compared
93 to very low frequency (VLF) data in the range of 10-30 kHz. However, a major drawback of the
94 RMT system is that it works in a narrow frequency band, which limits the depth penetration. This
95 limitation becomes more problematic at the presence of conductive water column or sediments,
96 which can for example hinder delineation of bedrock level and potential weakness zones within it
97 both of which have great implications for planning of underground infrastructures, reinforcements
98 used and excavation methods (Malehmir et al., 2015; Dehghannejad et al., 2017).

99

100 In a recent study by Wang et al. (2018), the boat-towed RMT data and lake-floor electrical
101 resistivity tomography (ERT) are jointly inverted to model the structures below the waterbody at
102 the Äspö Hard Rock Laboratory (HRL) site in southeastern Sweden. The resistivity models from
103 the 2D inversions delineated subsurface structures such as a major northeasterly directed fracture
104 system that is highly saturated with saline water. The presence of fracture zone is observed in the
105 HRL underground facility and also confirmed by boreholes. The limited depth penetration of the

106 RMT data is somehow compensated for in the inversion process by incorporation of the ERT data
107 that are acquired with a reasonably long array extent (Ronczka et al., 2017).

108

109 Employing controlled-source audio magnetotelluric (CSAMT) at lower frequencies in the range 1
110 to 10 kHz is a proper solution to increase the depth penetration and for a reasonably fast data
111 acquisition. The concept of controlled sources in magnetotelluric studies was originally developed
112 to improve the signal strength (Goldstein and Strangway, 1975), especially in areas close to
113 manmade infrastructures where the background noise level is considerably high. In the controlled-
114 source measurements, in order to meet the plane wave approximation, the source, which is either
115 an electric or magnetic dipole, should be sufficiently far enough from the measuring site. Zong
116 and Hughes (1991) give a detailed account on the CSAMT method and discuss the conditions for
117 near- and far-field electromagnetic data acquisition and interpretations. Wannamaker (1997)
118 provides perquisites for source-receiver separation to be 5 times the skin depth in order to avoid
119 near-field effects (NFE). Pedersen et al. (2005) and Bastani et al. (2009 and 2011) present the
120 results of RMT and CSAMT measurements for a number of near-surface investigations. Sterich
121 and Becken (2010) provide a detailed account on the EM fields from a finite-length wire source
122 and compare it with a point dipole solution. They discuss the issues caused by point source
123 approximation where the long wires of hundreds of meters are used to generate the EM signals.
124 Use of controlled source EM approaches for hydrocarbon exploration is discussed in detail by
125 Streich (2016). Saraev et al. (2017) present the use of controlled source radio-magnetotellurics
126 (CSRMT) for near surface investigations in remote regions. They demonstrate use of grounded
127 electric dipole as a source where they could measure the signal in a wide frequency range by
128 utilizing the odd harmonics of the base frequency. Shlykov and Saraev (2015) discuss and present

129 the possibilities of estimating the macro-anisotropy of the earth material from the RMT sounding
130 and using a controlled source that transmits the signals up to 1000 kHz. They also provide a
131 forward modelling solution that takes into account the displacement currents. Tezkan et al. (2019)
132 show an application of the CSRMT survey to detect and model the buried faults in 2D in Vuoska
133 region close to the city of St. Petersburg. The study included the CSRMT measurements using a
134 horizontal electrical dipole using the frequencies of 0.5, 11.5, 30, and 105 kHz and their odd
135 harmonics. They could successfully resolve and map the buried faults by using resistivity model
136 from the 2D inversion of the acquired CSRMT data. Synthetic analysis carried out by Mehta et al.
137 (2017) suggests that EM frequencies as low as 2.5 kHz should provide the desired penetration
138 depth in the case of Lake Mälaren site to gain better understanding of the fracture systems in the
139 underlying resistive bedrock. The logistical requirement to acquire CSAMT data on shallow
140 waterbodies with a floating platform is possible but challenging and can be time-consuming since
141 the measurement time at each station can take a few minutes. To keep the towed platform with
142 sensors stable at a location can also be difficult and impractical at places where ships and boats
143 can pass often and frequently. Wang et al. (2019) present the results of their study at HRL site
144 made in June 2017. They acquire boat-towed RMT and CSAMT data along a 600-m-long profile
145 to showcase the increased depth penetration when the lower frequency data in the range 1.25-12.5
146 kHz are included in the 2D inversions. The resulting resistivity models resolve the deeper parts of
147 the underlying fractured granite when compared to the inversion of just the RMT data. However,
148 in the presented case, the measurement platform is stationary and stabilized during the data
149 acquisition using a rope that is fixed to an island located in the middle of the profile. Such a
150 procedure slows the production rate and might not even be possible at many locations. Recently,
151 Shlykov et al. (2020) present an interesting application of the CSRMT method to map and model

152 permafrost in an area located at northern part of Siberia. By using the same data frequency range
153 presented in Tezkan et al. (2019) they could successfully delineate loam and sand horizons using
154 the resistivity models from the 2D inversion of the CSRMT where they also compared the results
155 with the existing borehole data. Yavich et al. (2020) present a new fast 3D parallel simulation code
156 applied to the CSRMT data acquired in Aleksandrovka study area in Kaluga Region, Russia. Their
157 results reveal that the developed method can be applied in the very complex geological structures.
158 In our case study, after a number of careful inspections, we took advantage of the Nordic winters
159 and carried out the simultaneous RMT and CSAMT measurements on the frozen lake of Mälaren
160 during February 2017. Hereafter we use the term CSRMT wherever the results from the
161 combination of both methods are presented to make the text more compact and easier to follow,
162 unless the RMT and CSAMT should separately be discussed.

163 The present study provides detailed information about the field procedures, source setup and data
164 processing of the CSRMT measurements made for the first time on a frozen lake along four parallel
165 profiles. 2D inversion results of the acquired CSRMT data demonstrates deeper penetrations down
166 to approximately 40-80 m depth, leading to a better delineation of the level and possible weakness
167 zones within the resistive granitic bedrock where the underwater planned tunnels will be running
168 through. The resistivity models from 2D inversion also better correspond with the existing marine
169 high-resolution reflection seismic data from the same site illustrating the accuracy and
170 effectiveness of the approach.

171

172 **Study area and survey setup**

173 The study area is located close to the city of Stockholm, Sweden. The measurements were
174 carried out over one of the three water passages (Figure 1) reported by Bastani et al. (2015). A

175 detailed account of the geology in the area is given in Mehta et al. (2017). The selected water
176 passage, number 2, is between the Lovön and Kungshatt islands (Figure 1). The bedrock at the
177 tunnel location is of granitic and partly metasedimentary rock types. Geological observations
178 indicate fractures in the crystalline bedrock that vary in width (1-5 m) and are partly filled with
179 clay, graphite, and chlorite. The CSRMT data were collected along four profiles (Figure 2) on
180 the frozen Lake Mälaren. All the four profiles are nearly parallel to each other and run in a SW-
181 NE direction. The distance between the profiles is approximately 50 m with station interval of 25
182 m and 24 stations per profile (a total length of ca 580 m). The frozen ice crust was about 10-15
183 cm at the time of the survey. Five holes were drilled to allow electrodes in contact with the lake
184 water (one for grounding and four for two electric components). These holes (in total 500) were
185 drilled using a handheld auger prior to the survey in order to allow faster station deployment.

186 **Data processing and quality**

187 The EnviroMT (Bastani, 2001) acquisition system was used to measure the EM signal. The setup
188 of the EnviroMT field equipment is similar to a typical MT set up as shown in Figure 3. The
189 magnetic sensor is composed of three induction coils and is placed in a way that the two
190 horizontal sensors measure the magnetic field components along and perpendicular to the profile
191 and the third one measures the vertical component. Two pairs of electric field sensors and the
192 horizontal magnetic field sensors are aligned either parallel or perpendicular to the profile
193 direction. The system acquires data in two modes, namely RMT and CSAMT. At each station,
194 the RMT data in the frequency range 14-250 kHz are acquired and stored first. Seven frequencies
195 are used after the processing and the transmitters during the acquisition are typically more than
196 20. Then the controlled-source signals, generated in the frequency range of 2.5-12.5 kHz are
197 recorded. In each measurement mode the data quality can be checked and if necessary, the data

198 at given mode/frequencies are repeated. The recorded data are the components of the EM field
 199 that are processed to estimate the complex-valued EM transfer functions, namely impedance
 200 tensor, \mathbf{Z} , defined as

$$201 \quad \begin{bmatrix} E_x \\ E_y \end{bmatrix} = \begin{bmatrix} Z_{xx} & Z_{xy} \\ Z_{yx} & Z_{yy} \end{bmatrix} \begin{bmatrix} H_x \\ H_y \end{bmatrix} \quad (1)$$

202 and tipper vector (also referred to as vertical magnetic transfer function), \mathbf{T} , given by

$$203 \quad H_z = [T_x \quad T_y] \begin{bmatrix} H_x \\ H_y \end{bmatrix} = \mathbf{T} \begin{bmatrix} H_x \\ H_y \end{bmatrix} \quad (2)$$

204 where E and H are the electric and magnetic field components, respectively. The subscripts x and
 205 y refer to directions of the sensors' setup in the field. In our case x was perpendicular and y in the
 206 profile direction. In the routine MT data interpretation, the input data for forward modelling and
 207 inversion are the tipper data calculated as in equation (2), apparent resistivity and the impedance
 208 phase at a given target frequency, f , in measurement directions, xy or yx , calculated as

$$209 \quad \rho_{xy/yx}(f) = \frac{|Z_{xy/yx}|^2}{2\pi\mu_0 f} \quad (3)$$

$$210 \quad \varphi_{xy/yx}(f) = \text{Arg}(Z_{xy/yx}) \quad (4)$$

211 where xy refers to the electric field in x direction and the magnetic field in y direction, vice versa
 212 for yx .

213 The field data processing schemes integrated into the EnviroMT is detailed in Bastani (2001). In
 214 the RMT mode, at every station the number of selected transmitters depends on the site location
 215 and a predefined signal to noise ratio (S/N) of the total horizontal magnetic field power. For the

216 Lake Mälaren survey, we used a threshold of 10 dB and on an average 24 radio transmitters were
217 selected. The stored raw data are mean stacked auto and cross powers of five components of the
218 measured EM fields at selected transmitter frequencies. The RMT transfer functions (**Z** and **T**)
219 are then estimated using the band averaging technique (Bastani, 2001). The uneven distribution
220 and lack of radio transmitters in certain frequency bands affect the quality of the estimated
221 transfer functions. Pederson et al. (2006) reports gaps in the spectrum of radio transmitters in
222 Europe. At the Lake Mälaren site we could observe these gaps. Two such gaps are visible in the
223 data (Figure 4).

224

225 The signal source for the CSAMT measurements consists of two orthogonal horizontal magnetic
226 dipoles. The source can remotely be controlled from the recording point. The location of the source
227 is shown in Figure 2 with a yellow square mark. Based on the results of previous studies (Mehta
228 et al., 2017), we selected 5 source frequencies of 2.5, 3.2, 5, 8 and 10 kHz. The source, when
229 triggered, activates one of the magnetic dipoles and the signal is transmitted according to the given
230 list of frequencies. The second dipole is then activated, and the same procedure is repeated (Bastani,
231 2001). Eventually, the tensor transfer functions and their corresponding errors are estimated with
232 a method given by Li and Pedersen (1991). As it is also discussed by Li and Pedersen (1991), at
233 certain distances from the transmitter site the data might contain EM signals that are not only
234 dependent on the induced currents in the earth electrical resistivity structure but also depend on
235 the type of the transmitter/source used. At large distances where the depth penetration of EM signal
236 is considerably smaller (5-10 times) than the distance to the source, the wave can be considered as
237 plane and the source effects are negligible. In the RMT case the EM waves are certainly plane, and
238 the data can be inverted using the standard 2D/3D MT programs. However, for the inversion of

239 combined RMT and CSAMT data one must ascertain that the later are measured at distances long
240 enough from the source where the plane-wave assumption is met. At closer distances/lower
241 frequencies, the source effects might be either considered (using the code that take the source
242 effects into account, for example see Wang et al., 2019) or the source contaminated data, namely
243 near field data, must be rejected prior to the inversion.

244

245 The collected data in our study show a smooth transition between the RMT and CSAMT
246 frequencies in both apparent resistivity and phase data. This provides an indication of CSAMT
247 data being in the far field. The typical signature of the near-field effect for a magnetic dipole source
248 in case of homogeneous half space is that with decreasing frequency the phase rises above 45
249 degrees and apparent resistivity decreases. In this study, the closest and farthest stations to the
250 source were at distances 477 m and 625 m, respectively, and the second closest station is 516 m
251 away from the source. At few stations on the northwestern part of the area, some signs of the near-
252 field effects (NFE) were observed in the raw data at lower frequencies. Most of the measuring
253 stations located at a distance greater than 500 m from the source did not show any NFE. An
254 example of raw data quality along profile C1 is shown in Figure 5. A smooth transition from the
255 RMT to CSAMT frequencies provides confidence to combine both datasets for further modeling
256 and interpretation. The controlled source data in YX direction show more sensitivity in detecting
257 a resistive structure at the deepest parts of the profile as compared to data in XY direction.
258 Especially, a decreasing phase in YX direction from values > 55 degrees to values below 45 nearly
259 along the entire profile indicates the presence of a resistive structure at depth. The phase in XY
260 direction shows nearly the same trend at the starting stations (1-10) and no sensitivity along the

261 rest of profile. The apparent resistivity data do not show clear indication of a resistive feature at
262 the lowest frequencies.

263 **2D inversion of combined RMT and CSAMT data**

264 As mentioned earlier, the most important objective to acquire the CSAMT data in the area (Figure
265 1) was to increase the depth of penetration using lower frequencies to the level where the planned
266 tunnels would be excavated. The CSRMT profiles are perpendicular to the boat-towed RMT
267 profiles (Bastani et al., 2015 and Mehta et al., 2017) and cover the area with the deepest water
268 column where the RMT signal may not reach the crystalline bedrock. This means that the measured
269 CSAMT data can be included in the inversion of the boat-towed RMT data to improve sensitivity
270 to the resistivity variations within the bedrock. We used EMILIA program (Kalscheuer et al., 2008;
271 Siripunvaraporn and Egbert, 2000) for the 2D inversion of the CSRMT data, which uses the finite
272 difference method for forward solver and Gauss-Newton method for the inversion. Mehta et al.
273 (2017) carried out strike and dimensionality analysis for the previously acquired RMT data and
274 showed that the geological strike is along the water passage, nearly perpendicular to the RMT
275 profiles. Thus, no rotation of the data collected in both campaigns was required. Joint transverse
276 electric (TE) and transverse magnetic (TM) mode inversions, namely TE+TM, were carried out
277 on the CSRMT dataset to obtain a better constraint on the deeper parts of the models (Pedersen
278 and Engels, 2005). In the TE mode, electric current flows along the strike direction. In the TM
279 mode, the electric current flows in the plane perpendicular to the strike direction. An error floor of
280 10% on the apparent resistivity and 5% ($\sim 2.86^\circ$) on the phase was used in the inversion. The design
281 of the model mesh was such that the shallowest block size was 0.5 m thick and the subsequent cell
282 thickness increased with geometrical progression factor of 1.12. The deepest cell thickness was
283 2500 m. We considered two blocks per measuring point for the horizontal dimensions of cells. We

284 used a homogeneous half space of $1000 \Omega\text{m}$ as the starting model. Regularization is used for
285 smoothness constraint in the inversion (Constable et al., 1987). The horizontal smoothness
286 weighting factor is equal to the vertical one, so that no preferred smoothness was given in any
287 direction.

288 The selected boat-towed RMT profile L9 (marked with an arrow in Figure 2) coincides with four
289 controlled-source stations. These two datasets were combined and inverted together. The inversion
290 was carried out with two steps: (1) the Occam inversion with the maximal data inclusion unless
291 the data point is too noisy to be accepted and (2) the damped Occam inversion with the data points
292 which have reasonable misfits. In the second step, the starting model is the best fitted model in the
293 first inversion. More details can be found in Wang et al. (2018). Besides, two lowest frequencies
294 (2.5 & 3.2 kHz) at the station closest to the source were omitted to eliminate the near-field effects.
295 For a conservative consideration, the distance between the source and receivers is required to be
296 12 times larger than the skin depth to avoid the near-field effect. Figure 6a shows the resistivity
297 model from joint inversion of TE+TM mode of only RMT data (boat-towed) along L9 (see Figure
298 2 for the location) with an RMS of 1.74. Figure 6b shows the results from the combined RMT and
299 CSAMT datasets with an RMS of 1.62. The detailed data misfits are also shown in Figure 7. TE-
300 mode apparent resistivities have relatively high misfit at 28.31 kHz in the middle of the profile.
301 TM-mode apparent resistivities have relatively high misfit at 226.50, 160.03, and 28.31 kHz in
302 the middle of the profile. However, the phase data in both modes have low misfits. The inverse
303 model has shallow structures well constrained by RMT data and deeper structures constrained by
304 CSAMT data (Figure 6). The major difference in the two models is in the middle of the profile
305 where a resistive feature below the conductive layer can be more clearly observed when CSAMT
306 data are included. The controlled-source data at stations located in the middle of the profile, where

307 the conductive marine sediments overlying the more resistive and partly fractured crystalline have
308 likely the greatest thickness, show considerable improvement in the model resolution at depth
309 thanks to the increased penetration depth. The penetration depth, white dashed lines in Figure 6,
310 was calculated as 1.5 times skin depth based on Spies (1989) and Huang (2005). The feature in the
311 model below the penetration depth is not reliable for interpretation.

312

313 **Reflection seismic data**

314 The reflection seismic data were acquired in a separate project and by another party (Nilsson,
315 2008). However, data in the form of raw shot gathers were made available to us for comparative
316 studies and supporting the current studies. The dataset covers the two water passages and was
317 acquired over the planned tunnels using a-12-channel hydrophone-streamer system positioned 0.5
318 m in the water. Hydrophones were separated 1 m. Boomer was used as the seismic source. A
319 sampling rate of 0.125 ms was used for the acquisition. The reflection data processing involved
320 mainly marine geometry setup, velocity analysis and stacking. No migration was attempted since
321 the dataset is quite shallow and that diffractions likely from undulated bedrock or fractured
322 bedrocks were intended to be kept for interpretations. Multiples while strong from both the lake
323 floor (sediments) and bedrock, they did not make trouble for this study as the target depths were
324 only a few meters in the bedrock and that multiples arrived much later in the dataset. The water
325 bottom and sediments bottom can clearly be seen in the reflection seismic section (Figure 6c).
326 Only two sections (S4 and S6) are presented together with CSRMT results in this study since the
327 main objective is to investigate the CSRMT survey results.

328 **Interpretation and discussion**

329 The resistivity model obtained from 2D inversion of only RMT dataset shows some distinct
330 resistive features (Figure 6a). The shallowest part of the model, mainly in the form of a 10-12 thick
331 layer with a resistivity of ca 200 Ω m, represents the freshwater. The large contrast between the
332 freshwater resistivity and the underlying lake sediments with considerably lower resistivity yields
333 the best-case scenario for the inversion to resolve the boundaries between the two, especially with
334 the inclusion of CSAMT data (Figure 6b). The water-sediment boundary also well correspond with
335 the strong reflection seen in the reflection seismic data (Figure 6c). The underlying more
336 conductive lake sediments layer has a varying thickness along the profile that seems to be generally
337 thinner on the NW and SE ends and thicker in the central part of the water passage. This limits the
338 depth penetration of the RMT signal and leads to the ambiguities to analyze the bedrock resistivity
339 variations by just using RMT resistivity models. However, the CSAMT data has less limit of
340 resolving the features in the bedrock.

341 Information available from a few cored boreholes in the area suggests the presence of fracture
342 systems with a varying width of a few centimeters to tens of centimeters within the bedrock, and
343 the total width of the fracture systems can reach up to 1-5 m (Ignea 2015; Mehta et al., 2017). The
344 dominating minerals within the fracture system are graphite, chlorite, and calcite. The resistivity
345 model in Figure 6a does not show any indication of such a lower-resistivity fracture system, which
346 is mainly because of poor data sensitivity (limited depth penetration, see in Figure 8a-b) and partly
347 smoothing imposed by the smoothness constraint used in the inversion. The new controlled-source
348 stations can make it possible to resolve the depth to bedrock at the middle of the profile where
349 thick lake sediment is present (Figure 8c-d). The near surface features interpreted in the RMT
350 model can be observed in the new CSRMT model as well (Figure 6b). The locations of controlled-

351 source stations are marked along the x-axis with stars. The resistivity model differs from the RMT
352 model mainly at the depth in the distance 100-200 m along the profile where a more resistive
353 feature can be observed. Clearly, the sediments lower boundary is focused, and the fractured zone
354 in the bedrock is detected when the controlled source data are added. According to the borehole
355 information, the depth to the fractured bedrock (or the bottom of lake sediments) is expected to be
356 about 30-50 m which seems to be better resolved with control source lower frequencies. Noticeably,
357 the resistivity of the fractured bedrock appears to be relatively low. This can be probably caused
358 by the presence of infilling of conductive materials and clays in the fracture system.

359 The acquired reflection seismic data closest to the RMT profile L9 is presented in Figure 6c. A
360 major undulation in the seismic section (S4) can be observed (distances 150-200 m) that likely
361 marks the location where the bedrock might be eroded and can be inferred to be fractured. The
362 CSRMT model is superimposed on the seismic section and shown in Figure 6d. The undulations
363 in the bedrock can be easier compared and show a clear correlation between the two datasets that
364 are independently processed and modelled. Based on the estimate of skin depth and the distance
365 between the transmitter and receivers, the first controlled-source station towards the NW part of
366 the profile might be influenced by near-field effect (transmitter-reciever distance less than 12 times
367 of skin depth). Since the near-field effect is more dominant at lower frequencies, the two lowest
368 frequencies (2.5 and 3.2 kHz) were omitted from the dataset prior to the inversion to eliminate
369 effect. Sensitivities for the boundary of sediments and bedrock (anomaly A in Figure 8) and the
370 potential fracture zone (anomaly B in Figure 8) are studied by model perturbation. This means that
371 we have changed the resistivity of the model bounded in the region of anomaly A and calculated
372 the forward response of the model and compared the data fits with the resistivity model from the
373 inversion shown in Figure 6b. The resistivity of the anomalies is increased to 1000 Ω m from the

374 inverted values. The RMS increase is the original and perturbed RMS difference normalized by
375 the original RMS. For both anomalies, the RMS increases of combined inversions are nearly 2-3
376 times larger than the ones of RMT inversions, which indicates the increase of sensitivity at depths
377 due to the inclusion of four CSAMT stations. Clearly, the sensitivity tests not only show the low
378 frequency CSAMT signals increase the investigation depth of the inverse models, but also
379 illustrate that observed data have sensitivities to the bedrock surface and potential fracture zone
380 filled with conductive materials (Figure 8). One should note that the most conductive deepest zone
381 in Figure 6b at distances 150-200 m lies below depth of investigation and therefore our
382 interpretation of the possible fracture zone (marked by white lines in Figure 6d) are limited to
383 depths dictated by the depth of investigation.

384

385 To further scrutinize the effectiveness of the CSRMT survey on the frozen lake we show a
386 comparison between the resistivity model along profile L13 and the available reflection seismic
387 data along S6 (Figure 9). Even though this profile is away from our most interested region, it can
388 repeatedly demonstrate the improvements obtained by including the CSAMT data in the inversion.
389 The corresponding data misfits for the inversion are shown in Figure (10). Again, phase data have
390 lower misfits than the apparent resistivity data, and apparent resistivity data only have relatively
391 high misfits at certain frequencies. In both RMT and CSRMT models, water column is perfectly
392 resolved; However, bedrock undulation is only resolved in the CSRMT model. Resistivity of the
393 fracture system is relatively low due to the filling of conductive materials. Penetration depth, white
394 dashed lines in Figure 9, also shows that the discussed features are well constrained by the
395 observed CSRMT data. We must emphasize that the smoothing regularization applied in the
396 inversion, and the diffusive nature of EM fields in the earth, generate smoother nearly vertical low

397 resistivity zones compared to the observed fractures in the drillholes (reported by Ignea, 2015) that
398 are much narrower and have varying dips. But, comparing to the reflection seismic section, the
399 CSRMT data still have good vertical resolution.

400 **Conclusions**

401 To the best of our knowledge, for the first time, CSRMT data over a frozen lake were successfully
402 acquired in an area close to Stockholm and in connection to the planned bypass multi-lane
403 underground road tunnel project. The goal was to map the depth to bedrock and investigate the
404 presence of any fracture system particularly in the middle of the surveyed profiles where the
405 previously acquired boat-towed RMT dataset was incapable of resolving such details. Variation of
406 the modelled resistivity well correlates with the results reported in the previous studies, available
407 drillholes and reflection seismic data. This is also testified by the penetration depth evaluation,
408 inversion misfit analysis, and the model sensitivity by model perturbation method. Quality of the
409 CSRMT data collected are in general good although at some stations closer to the transmitter near-
410 field effect was speculated. In a broader perspective, the idea of CSRMT study on frozen lake can
411 be used on shallow waterbodies in similar climatic conditions where only RMT dataset is not
412 sufficient in terms of penetration depth. A more detailed analysis can be made by 3D
413 modelling/inversion of all densely collected RMT and CSRMT data in this survey area for future
414 studies. We anticipate this approach to open new opportunities in the northern countries for
415 infrastructure planning projects where these structures are expected to cross waterbodies and for
416 mineral exploration where little is known about subsurface structures and bedrock. However, the
417 Bayesian inversion could be used in the further along the full CSRMT profiles for quantitative
418 model uncertainty studies, which is hard to achieve with deterministic inversions, such as the one
419 we used.

420

421 **References**

- 422 Andersson, M., Malehmir, A., (2018) Unravelling the internal architecture of the Alnö alkaline
423 and carbonatite complex (central Sweden) using 3D models of gravity and magnetic data.
424 *Tectonophysics*, 740– 741, 53–71.
- 425 Bastani, M., (2001) EnviroMT – A New Controlled Source /Radio Magnetotelluric System. PhD
426 thesis: Acta Universitatis Upsaliensis, *Uppsala Dissertations from the Faculty of Science and*
427 *Technology* 32.
- 428 Bastani, M., Persson, L., Mehta, S., Malehmir, A., (2015) Boat-towed radio-magnetotellurics
429 (RMT) - a new technique and case study from the city of Stockholm, *Geophysics*, 80, B193–
430 B202.
- 431 Bastani, M., Savvaidis, A., Pedersen, L.B., Kalscheuer, T., (2011) CSRMT measurements in the
432 frequency range of 1–250 kHz to map a normal fault in the Volvi basin, Greece, *Journal of*
433 *Applied Geophysics*, 75, 180–195, doi:10.1016/j.jappgeo.2011.07.001.
- 434 Constable, S.C., Parker, R.L. and Constable, C.G., 1987. Occam's inversion: A practical
435 algorithm for generating smooth models from electromagnetic sounding data. *Geophysics*,
436 52(3), 289-300.
- 437 Dugan, H.A., Arcone, S.A., Obryk, M.K., Doran, P.T., (2016) High-resolution ground-
438 penetrating radar profiles of perennial lake ice in the McMurdo Dry Valleys, Antarctica:
439 Horizon attributes, unconformities, and subbottom penetration: *Geophysics*, 81, (1), WA13-
440 WA20. <https://doi.org/10.1190/geo2015-0159.1>

- 441 Dugan, H. A., Doran, P. T., Tulaczyk, S., Mikucki, J.A., Arcone, S.A., . Auken, E., Schamper, C.,
442 Virginia, R. A., (2015) Subsurface imaging reveals a confined aquifer beneath an ice-sealed
443 Antarctic lake: *Geophysical Research Letters*, 42, 96–103, doi: 10.1002/2014GL062431.
- 444 Goldstein, M. A., Strangway, D. W., (1975) Audiofrequency magnetotellurics with a grounded
445 electric dipole source, *Geophysics*, 40, 669–683.
- 446 Huang, H., (2005) Depth of investigation for small broadband electromagnetic sensors,
447 *Geophysics*, 70, (6), G135–G142.
- 448 Ignea, S., (2015), Major Fracture Zones in Fiskarfjärden, Stockholm, M.Sc thesis, *Uppsala*
449 *Universitet*, ISSN 1650-6553 Nr 323.
- 450 Kalscheuer, T., Pedersen, L.B., Siripunvaraporn, W., (2008) Radiomagnetotelluric two-
451 dimensional forward and inverse modelling accounting for displacement currents, *Geophysical*
452 *Journal International*, 175, 486–514, doi: 10.1111/j.1365-246X.2008.03902.x.
- 453 Li, X., Pedersen, L.B., (1991), Controlled source tensor magnetotelluric, *Geophysics*, 56, 1456-
454 1461.
- 455 Mehta, S., Bastani M., Malehmir, A., Pedersen, L.B., (2017) Resolution and sensitivity of boat-
456 towed RMT data to delineate fracture zones—example of the Stockholm bypass multi-lane
457 tunnel, *Journal of Applied Geophysics*, 139C, 131–143, DOI: 10.1016/j.jappgeo.2017.02.012.
- 458 Nilsson, P., (2008) Sjömätningar i tre passager under Mälaren, Förbifart Stockholm Teknisk
459 Rapport Nr 2008–11, GeoNova Consulting AB, Sweden (www.geonovaconsulting.se).
- 460 Pedersen, L.B., Bastani, M., Dynesius, L., (2005) Groundwater exploration using combined
461 controlled-source and radiomagnetotelluric techniques, *Geophysics*, 70, G8–G15.

- 462 Pedersen, L. B., Bastani, M., Dynesius, L., (2006) Radiotransmitters in Europe and their use in
463 high resolution geophysical exploration of near-surface geology, *Geophysics*, 71, (6), G279–
464 G284.
- 465 Pedersen, L.B. and Engels, M., (2005) Routine 2D inversion of magnetotelluric data using the
466 determinant of the impedance tensor, *Geophysics*, 70, 31–41.
- 467 Persson, L., (2001) Plane Wave Electromagnetic Measurements for Imaging Fracture Zones, PhD
468 thesis. Acta Universitatis Upsaliensis, *Uppsala Dissertations from the Faculty of Science and*
469 *Technology* 30.
- 470 Spies, B.R., (1989) Depth of investigation in electromagnetic sounding methods. *Geophysics*, 54, (7), 872–
471 888.
- 472 Ronczka, M., Hellman, K., Günther, T., Wisen, R., Dahlin T., (2017), Electric resistivity and
473 seismic refraction tomography: a challenging joint underwater survey at Äspö Hard Rock
474 Laboratory, *Solid Earth*, 8, 671–682, <https://doi.org/10.5194/se-8-671-2017>
- 475 Siripunvaraporn, W., Egbert, E. (2000) An efficient data-subspace inversion method for 2D
476 magnetotelluric data, *Geophysics*, 65, 791–803.
- 477 Pous, J., Poyatos, D.M., Heise, W., Santos, F.M., Zaldívar, J.G., Ibarra, P., Pedrera, A., Constán,
478 A.R., Anahnah, F., Gonçalves, R., Mateus, A., (2011) Constraints on the crustal structure of
479 the internal Variscan Belt in SW Europe: A magnetotelluric transect along the eastern part of
480 Central Iberian Zone, Iberian Massif, *Journal Geophysical Research*, 116, B02103,
481 doi:10.1029/2010JB007538.
- 482 Saraev, A., Simakov, A., Shlykov, A., & Tezkan, B., (2011) Controlled-source
483 adiomagnetotellurics: a tool for near surface investigations in remote regions. *Journal of*
484 *Applied Geophysics*, 146(2017), 228–237.

- 485 Shlykov, A. A., Saraev, A. K., (2015) Estimating the macroanisotropy of a horizontally layered
486 section from controlled- source radiomagnetotelluric soundings. *Izvestiya, Physics of the Solid*
487 *Earth*, 51(4), 583–601.
- 488 Shlykov, A., Saraev, A., Tezkan, B. Study of a Permafrost Area in the Northern Part of Siberia
489 Using Controlled Source Radiomagnetotellurics. *Pure Appl. Geophys.* 177, 5845–5859 (2020).
490 <https://doi.org/10.1007/s00024-020-02621-x>.
- 491 Streich, R., Becken, M., (2010) Electromagnetic fields generated by finitelength wire sources:
492 comparison with point dipole solutions: *Geophysical Prospecting*, 59, 361– 374.
- 493 Streich, R., (2016) Controlled-source electromagnetic approaches for hydrocarbon exploration and
494 monitoring on land: *Surveys in Geophysics*, 37, 47–80.
- 495 Tezkan, B., Hordt, A., Gobashy, M. (2000) Two-dimensional radiomagnetotelluric investigation
496 of industrial and domestic waste sites in Germany, *Journal of Applied Geophysics*, 44, 237–
497 256.
- 498 Turberg, P., Muller I., Flury, F., (1994) Hydrogeological investigation of porous environments by
499 audiometalluric resistivity, *Journal of Applied Geophysics*, 31, 133–143.
- 500 Tezkan, B., Muttaqien, I., Saraev, A, (2019). Mapping of buried faults using the 2D modelling of
501 far-field controlled source radio magnetotelluric data. *Pure and Applied Geophysics*, 176, 751–
502 766.
- 503 Ugalde H., Heureux, E. L, Lachapelle, R., Milkereit, B., (2006) Measuring gravity on ice: An
504 example from Wanapitei Lake, Ontario, Canada: *Geophysics*, 71, (3), J23–J29, doi:
505 10.1190/1.2189387
- 506 Yavich N., Malovichko M., Shlykov A., 2020 Parallel Simulation of Audio- and Radio-
507 Magnetotelluric Data. *Minerals*, 10, (1):42. <https://doi.org/10.3390/min10010042>

508 Wang, S., Kalscheuer, T., Bastani, M., Malehmir, A., Pedersen, L. B., Dahlin, T., & Meqbel, N.
509 (2018). Joint inversion of lake-floor electrical resistivity tomography and boat-towed radio-
510 magnetotelluric data illustrated on synthetic data and an application from the Äspö Hard Rock
511 Laboratory site, Sweden. *Geophysical Journal International*, 213, (1), 511-533.
512 <https://doi.org/10.1093/gji/ggx414>

513 Wang S., Bastani, M., Constable, S., Kalscheuer, T., Malehmir, A., (2019) Boat-towed radio-
514 magnetotelluric and controlled-source audio-magnetotelluric study to resolve fracture zones at
515 Äspö Hard Rock Laboratory site, Sweden, *Geophysical Journal International*, 218, (2), 1008–
516 1031, <https://doi.org/10.1093/gji/ggz162>

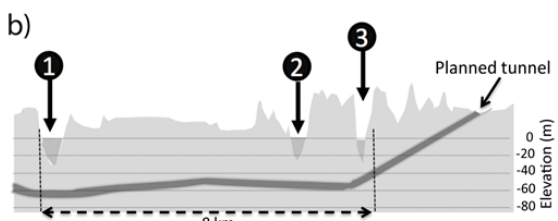
517 Wannamaker, P.E., (1997) Tensor CSAMT survey over the sulphur springs thermal area, Valles
518 Caldera, New Mexico, USA, Part II. Implications for CSAMT methodology, *Geophysics*, 62,
519 466–476.

520 Zonge, K.L., Hughes, L.J., (1991) Controlled source audio-frequency magnetotellurics.
521 *Electromagnetic Methods in Applied Geophysics*. V.2 - Applications. Series: Investigations in
522 Geophysics 3, pp. 713–809.

523

524 **Figures**

525 **Figure 1**



526

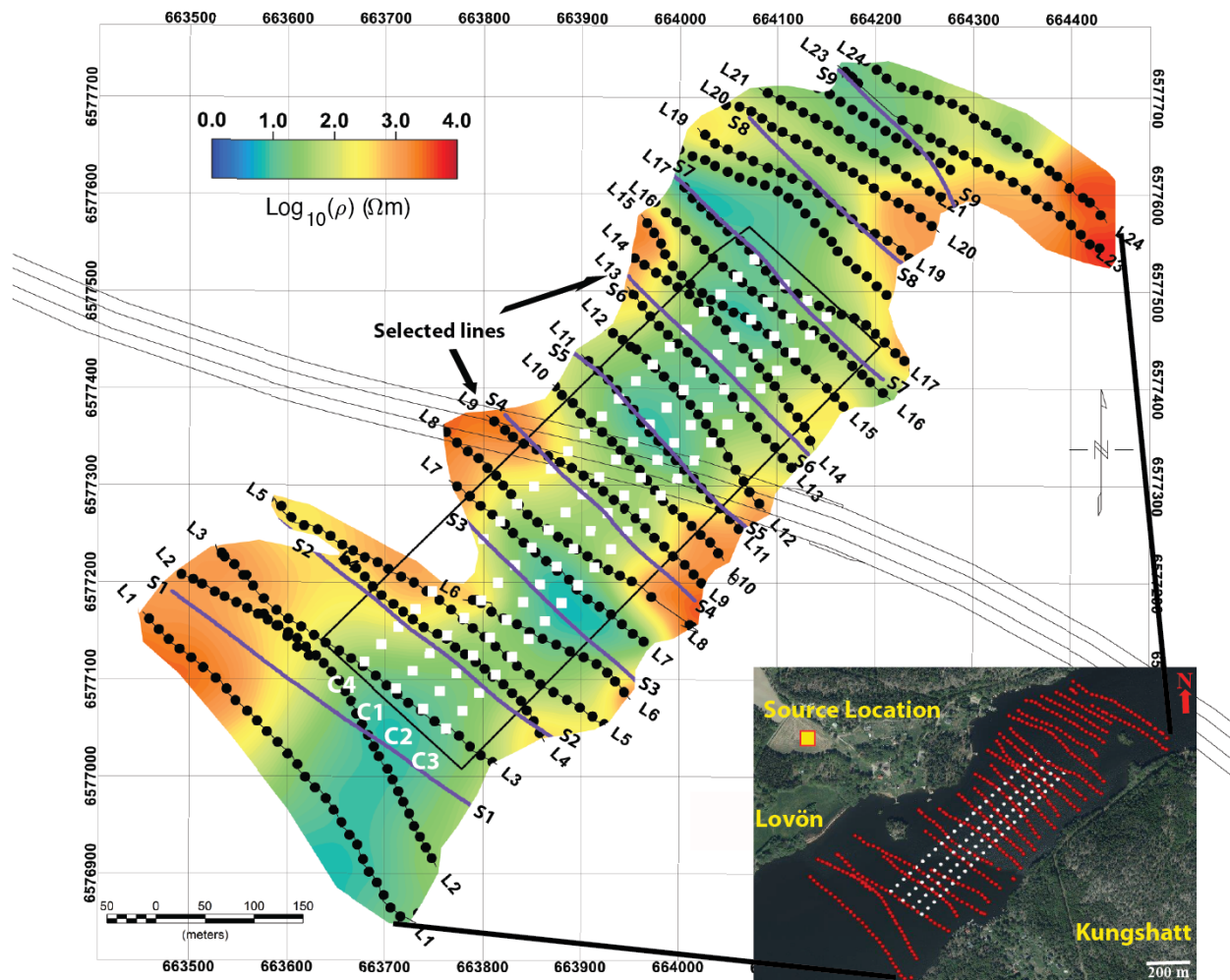
527

528

529

530

531 Figure 2



532

533

534

535

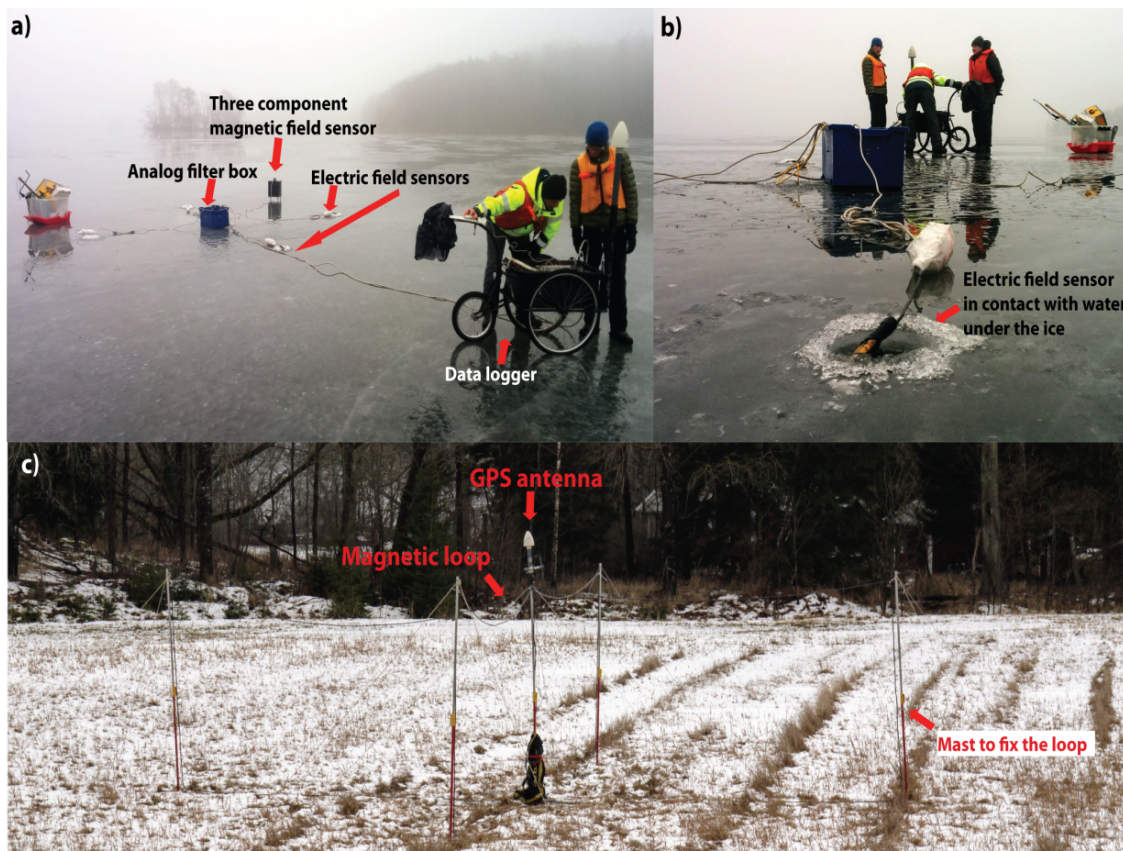
536

537

538

539

540 **Figure 3**



541

542

543

544

545

546

547

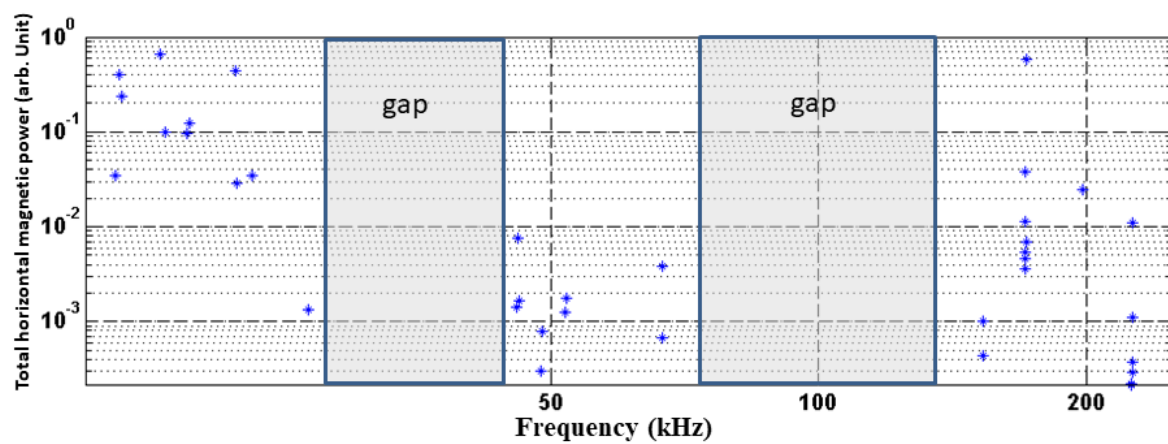
548

549

550

551

552 **Figure 4**



553

554

555

556

557

558

559

560

561

562

563

564

565

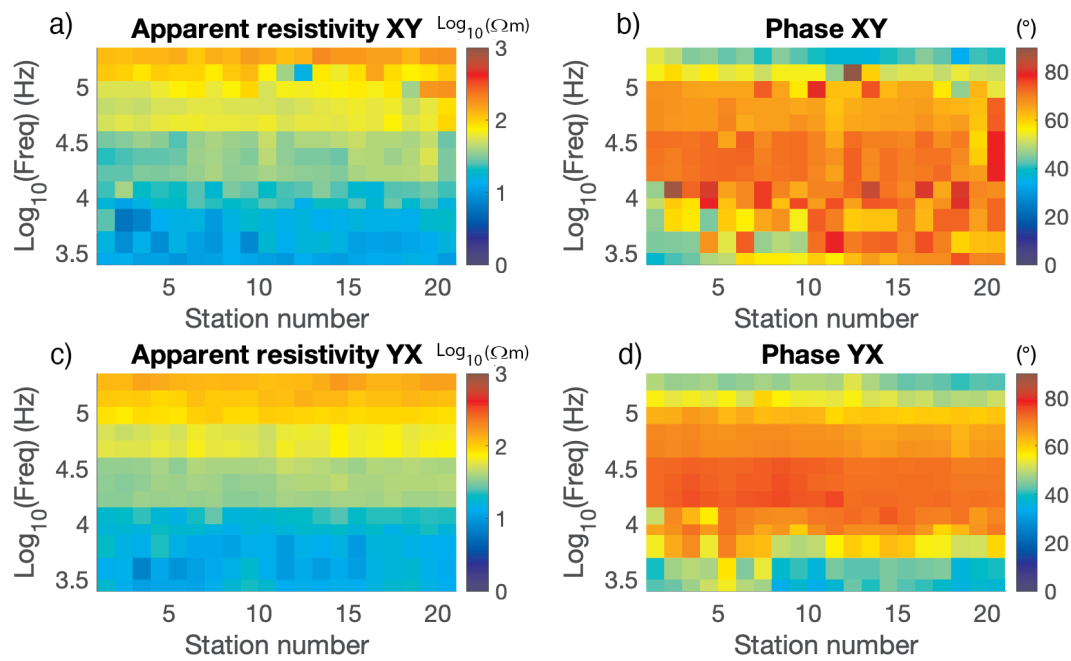
566

567

568

569

570 Figure 5



571

572

573

574

575

576

577

578

579

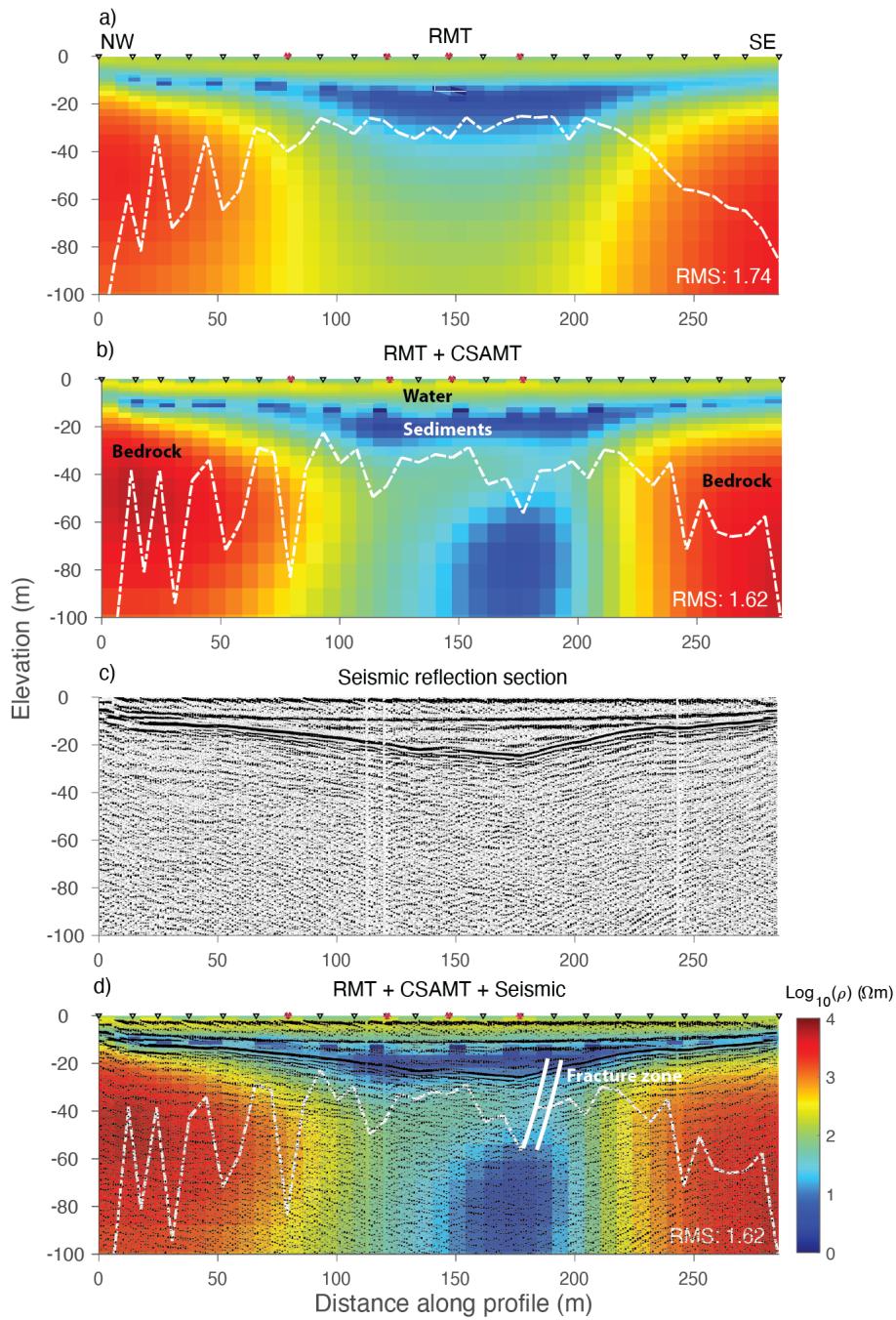
580

581

582

583

584 Figure 6



585

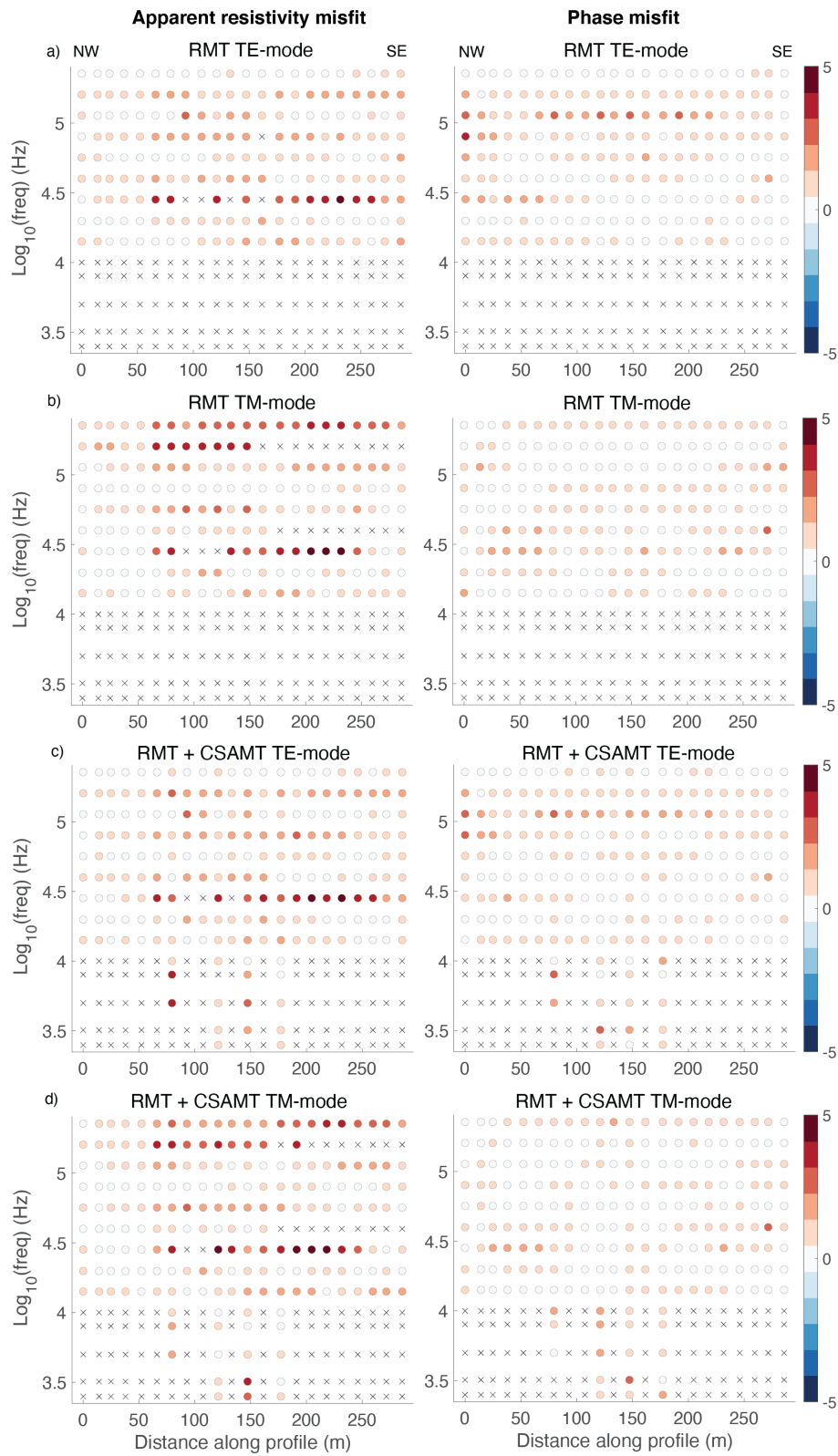
586

587

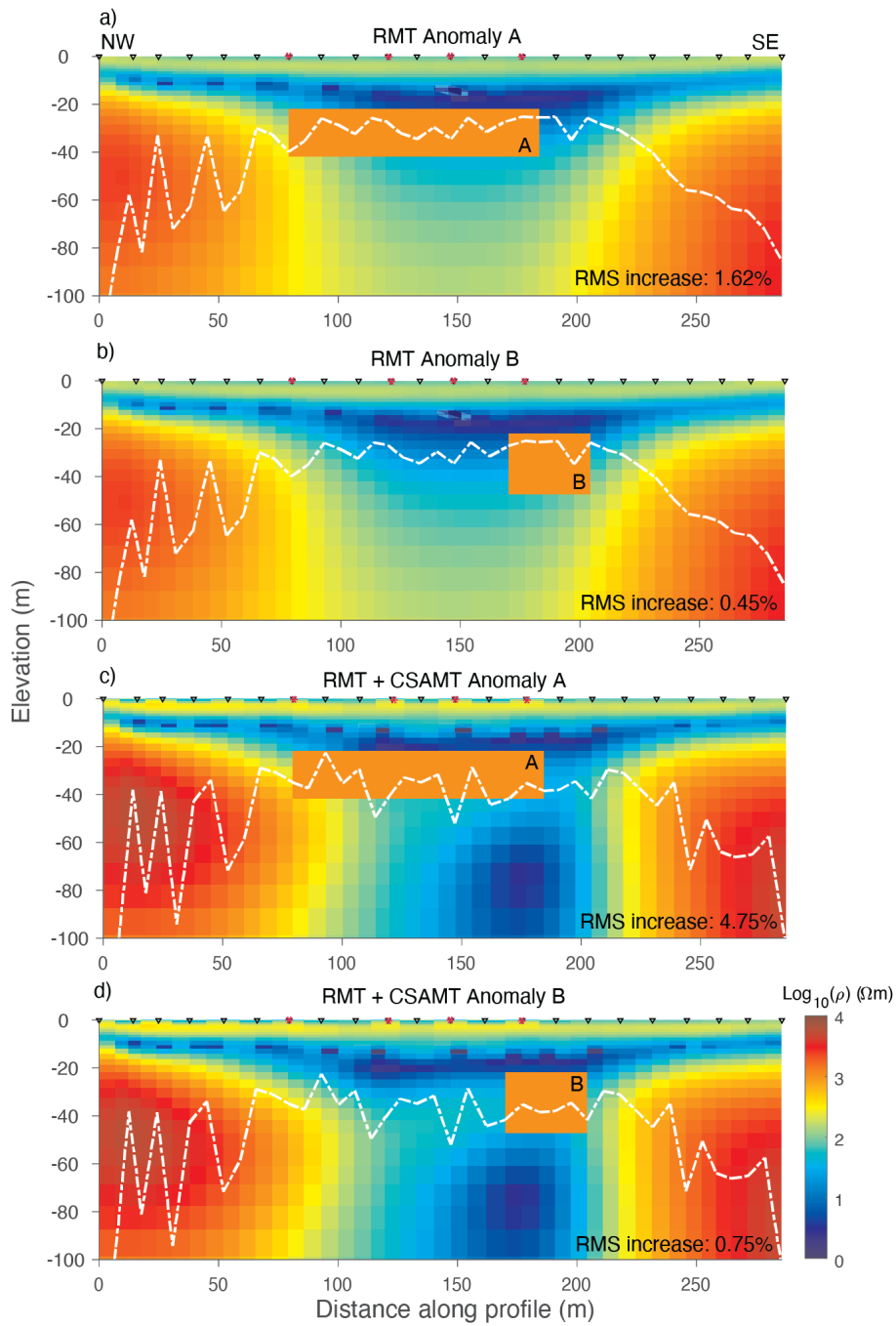
588

589

590 Figure 7



592 Figure 8



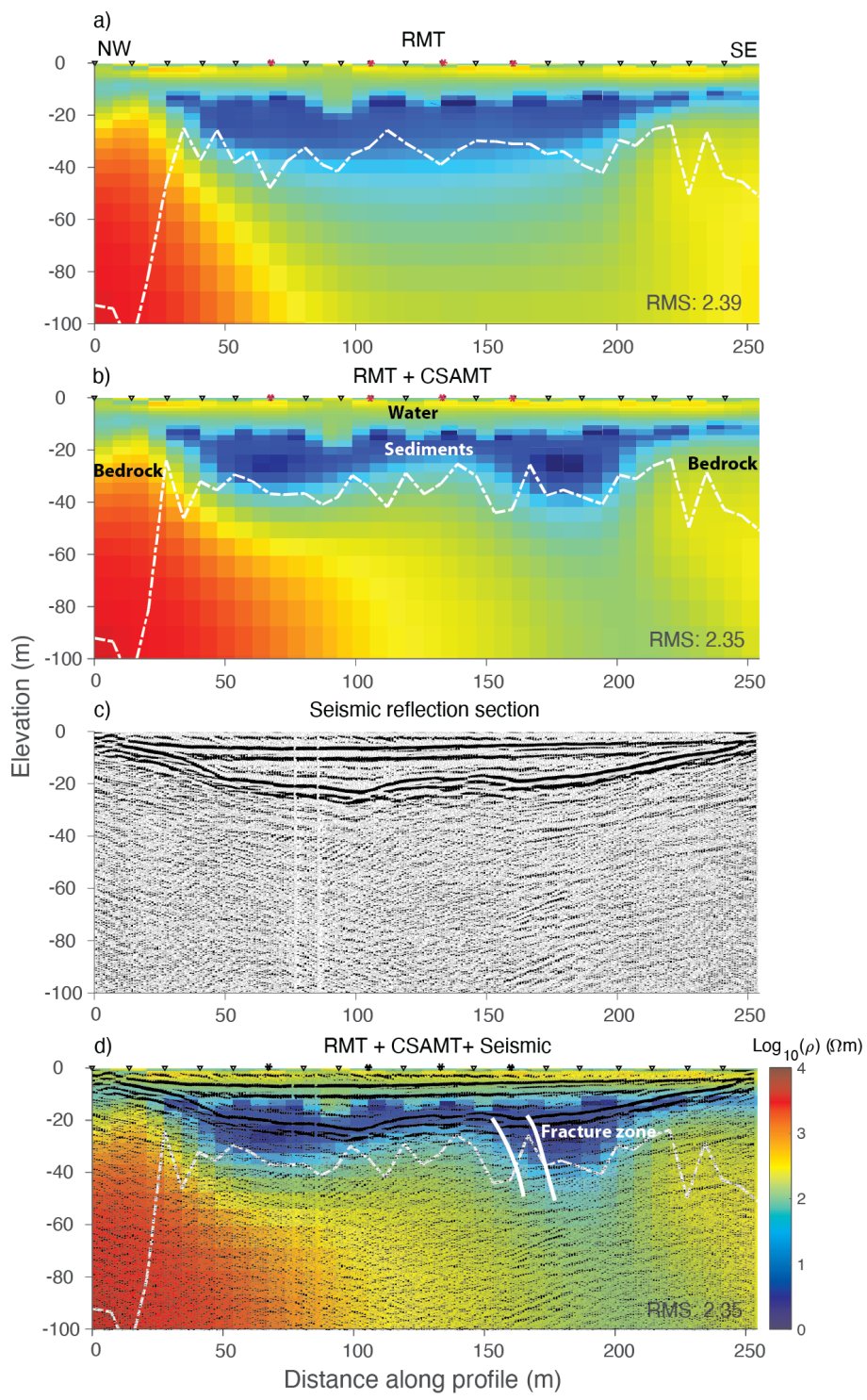
593

594

595

596

597 Figure 9

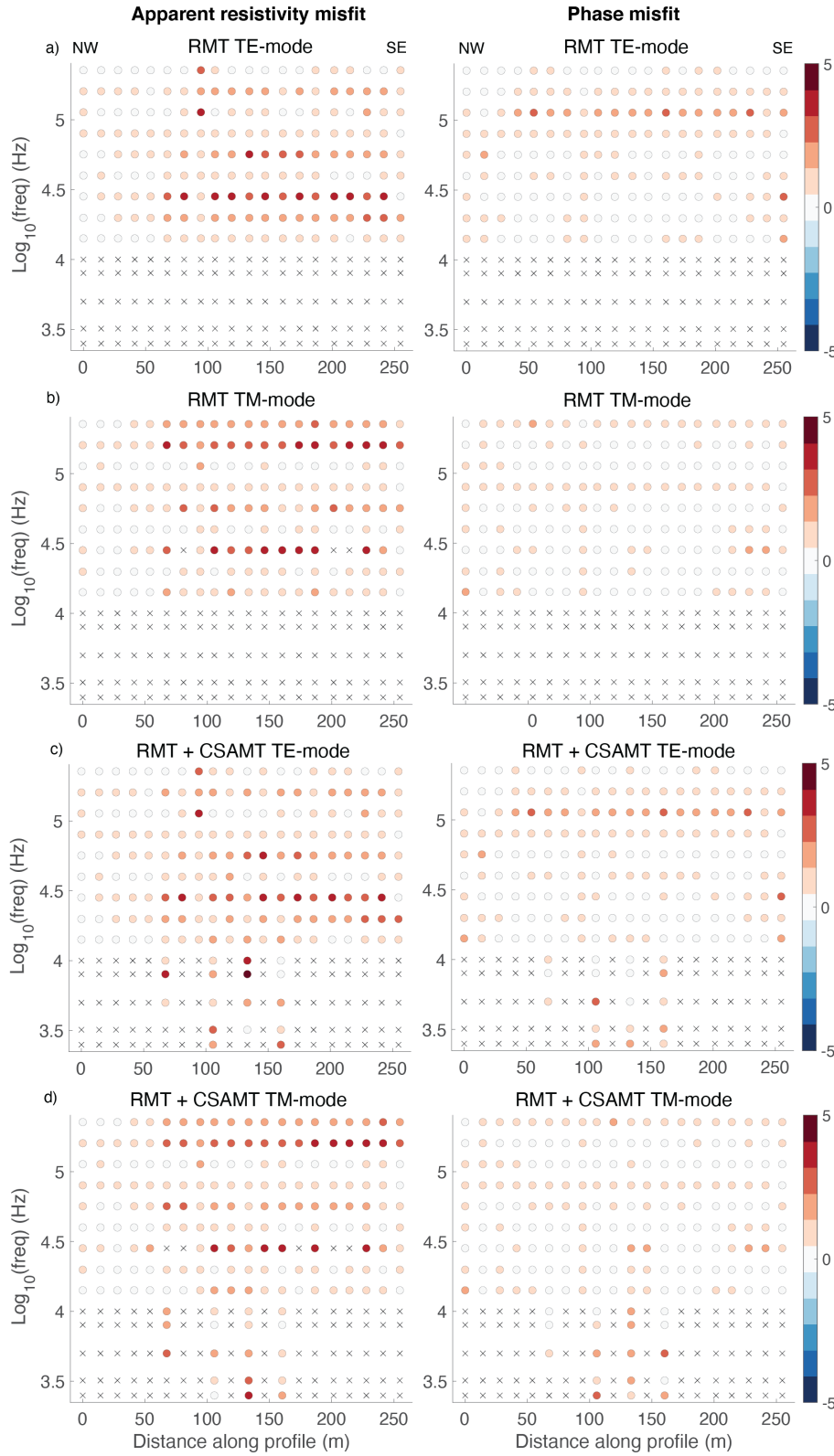


598

599

600

601 Figure 10



602

603

604 **Figure legends:**

605 Figure 1: Location of study area. (a) The Stockholm Bypass (Förbifart) project. The planned
606 bypass is shown with the green track. (b) Profile section of water passages, marked by numbers 1
607 to 3, showing the location and depths to the top of the tunnel. The inset map in (a) shows the
608 location of study area in Sweden.

609

610 Figure 2: Location of the boat-towed RMT profiles (marked from L1 to L24 with black circles and
611 lines) and the new CSRMT profiles (marked from C1 to C4 with white rhombus). In the
612 background the resistivity slice at 38 m depth from the 2D inversion of boat-towed RMT data are
613 shown (Mehta et al., 2017). In the present study and to showcase the improvements, we used L9
614 RMT profile (marked with arrow) along with the four controlled-source stations that located along
615 it. The location of the CSRMT source is shown in the inset figure (bottom right) with respect to
616 the previously acquired RMT and the newly acquired CSRMT stations.

617

618 Figure 3: (a) Photo showing the EnviroMT CSRMT field setup while measuring on the Lake
619 Mälaren near the city of Stockholm, Sweden. Different components of the setup are also shown.
620 (b) A close look at the drill hole made in the ice crust for proper electric electrode contact with
621 water. (c) The setup of the double magnetic dipole transmitter used as source.

622

623 Figure 4: Amplitude of the power spectra (unit is arbitrary) of radio transmitters at station 6
624 profile 1. The grey boxes show the gaps in the RMT frequency range.

625

626

627 Figure 5: Measured apparent resistivity and phase of CSRMT data at stations along profile C1. (a)
628 Apparent resistivity in XY direction, (b) phase in XY direction, (c) apparent resistivity in YX
629 direction, (b) phase in YX direction. At most stations the transition between RMT and controlled-
630 source data is smooth.

631

632 Figure 6: 2D inversion models of (a) RMT and (b) combined RMT and CSAMT dataset from L9
633 line shown in Figure 1. The location of the controlled-source stations along the profile is marked
634 by red ‘*’ in (b), and the location of RMT station is marked by inverse triangles. (c) For comparison
635 a nearly collocated reflection seismic section along the resistivity profile is superimposed (d) into
636 the model shown in (b). The improvement is significant especially in better delineating bedrock
637 level and its undulation on the middle part of the profile. Penetration depth of data is marked in
638 white dashed line, and the potential fracture zone is marked in white line.

639

640 Figure 7: Data misfits corresponding the inversion in Figure 6, which are the observed and
641 modelled data difference normalized by the data errors. In general, phase data have lower misfits
642 than the apparent resistivity data. The crosses mean the exclusion of data points in the
643 corresponding inversions.

644

645 Figure 8: Sensitivity test of anomaly A and anomaly B. The resistivity of the anomalies is
646 increased to 1000 Ωm from the inverted values for model perturbation. The RMS increase is the
647 original and perturbed RMS difference normalized by the original RMS. (a) Anomaly A for
648 RMT inversion, (b) anomaly B for RMT inversion, (c) anomaly A for RMT plus CSAMT
649 inversion, and (d) anomaly B for RMT plus CSAMT inversion. The RMS increases of RMT plus

650 CSAMT inversions are about 2-3 times larger than the ones of RMT inversions, which indicates
651 the increase of sensitivity at depths due to the inclusion of four CSAMT stations.

652

653 Figure 9: 2D inversion models of (a) RMT and (b) combined RMT and CSRMT dataset from L13
654 line shown (see Figure 2 for locations) and the location of the controlled-source stations along the
655 profile is marked by red '*' . (c) Reflection seismic data along the same profile. (d) For comparison
656 the nearly collocated reflection seismic section along the resistivity profile is superimposed on the
657 resistivity model shown in (b). Penetration depth of data is marked in white dashed line.

658

659 Figure 10: Data misfits corresponding the inversion in Figure 9, which are the observed and
660 modelled data difference normalized by the data errors. In general, phase data have lower misfits
661 than the apparent resistivity data. The crosses mean the exclusion of data points in the
662 corresponding inversions.

663